Cortical norepinephrine-astrocyte signaling critically mediates learned behavior

Authors: Gabrielle T. Drummond[1], Arundhati Natesan[1], Marco Celotto[1,2], Jennifer Shih[1], Prachi Ojha[1], Yuma Osako[1], Jiho Park[1], Grayson O. Sipe[3], Kyle R. Jenks[1], Vincent Breton-Provencher[4], Paul C. Simpson[5], Stefano Panzeri[2], Mriganka Sur[1*]

Affiliations:

[1] Department of Brain and Cognitive Sciences, Picower Institute for Learning and Memory, Massachusetts Institute of Technology, Cambridge, MA, 02139, USA

[2] Institute of Neural Information Processing, Center for Molecular Neurobiology (ZMNH), University Medical Center Hamburg-Eppendorf (UKE), 20251 Hamburg, Germany

[3] Department of Biology, Eberly College of Science and Huck Institutes of the Life Sciences, Pennsylvania State University, University Park, PA 16802, USA

[4] Department of Psychiatry and Neuroscience, CERVO Brain Research Center, Université Laval, Québec City, Québec, Canada

[5] Department of Medicine and Research Service, San Francisco Veterans Affairs Medical Center and Cardiovascular Research Institute, University of California, San Francisco, CA 94143, USA

*Corresponding author. Email: msur@mit.edu

Abstract:

Updating behavior based on feedback from the environment is a crucial means by which organisms learn and develop optimal behavioral strategies[1–3]. Norepinephrine (NE) release from the locus coeruleus (LC) has been shown to mediate learned behaviors[4–6] such that in a task with graded stimulus uncertainty and performance, a high level of NE released after an unexpected outcome causes improvement in subsequent behavior[7]. Yet, how the transient activity of LC-NE neurons, lasting tens of milliseconds, influences behavior several seconds later, is unclear. Here, we show that NE acts directly on cortical astrocytes via Adra1a adrenergic receptors to elicit sustained increases in intracellular calcium. Chemogenetic blockade of astrocytic calcium elevation prevents the improvement in behavioral performance. NE-activated calcium invokes purinergic pathways in cortical astrocytes that signal to neurons; pathway-specific astrocyte gene expression is altered in mice trained on the task, and blocking neuronal adenosine-sensitive A1 receptors also prevents post-reinforcement behavioral gain. Finally, blocking either astrocyte calcium dynamics or A1 receptors alters encoding of the task in prefrontal cortex neurons, preventing the post-reinforcement change in discriminability of rewarded and unrewarded stimuli underlying behavioral improvement. Together, these data demonstrate that astrocytes, rather than indirectly reflecting neuronal drive, play a direct, instrumental role in representing task-relevant information and signaling to neurons to mediate a fundamental component of learning in the brain.

Main Text:

Astrocytes are the major non-neuronal cell type in the cortex and are increasingly recognized as key contributors to the development, plasticity and function of neuronal circuits[8–12]. While astrocyte signaling has historically been considered as secondary to neuronal computations, recent work suggests a more central role for astrocytes in mediating switches in behavioral state via their responses to neuromodulatory inputs[13–16]. Yet, how they dynamically shape cortical circuits underlying learning and learned behavior is poorly understood. One potential mechanism is through their response to the release of neuromodulators; astrocytes respond robustly to norepinephrine (NE)[13,14,16–20] suggesting a specific role in NE-dependent learning and behavior. Furthermore, astrocyte calcium dynamics range from hundreds of milliseconds to several seconds[21–25], suggesting that these signals can reflect as well as influence neuronal activity and behavior on a range of time scales.

While goal-directed learning has classically invoked striatal dopamine signaling, it is known that NE is a critical mediator of state-dependent behavior[4–6] likely through its effects on

cortical processing[26–30]. The mechanisms by which NE influences neuronal activity in cortex during learned behavior are unknown. It has recently been shown that in a reinforcement learning task, NE-releasing neurons in the locus coeruleus (LC) project post-reinforcement signals to diverse cortical targets[7]. After especially unexpected outcomes, high LC-NE activity causes changes in behavior on the subsequent trial, as a substrate of online trial-by-trial learning and consistent with the hypothesis that NE acts as a global model failure signal[6]. The timescale of phasic LC-NE activity is extremely short (lasting tens of milliseconds), but the subsequent effects on behavior require that it is propagated for at least several seconds. How a brief prediction error signal is sustained to cause changes in behavior on longer time scales is unclear. Here, we show that cortical astrocytes are selectively responsive to NE released after an unexpected outcome, and that their prolonged calcium dynamics are causally related to behavioral updating on the next trial. NE-driven astrocyte modulation of behavior is dependent on purinergic signaling to neurons, which alters neuronal stimulus encoding on trials following an error and consequent negative reinforcement. Thus, astrocytes have an essential role in learned behavior: they integrate specific learning signals and modulate neuronal activity to mediate behavioral optimization.

Astrocytes exhibit sustained increases in calcium following an unexpected outcome

To evaluate the potential role of astrocytes in learned behavior, we trained mice in a go/no-go task with graded auditory stimulus evidence where animals must push a lever at a go tone to receive a water reward and refrain from pushing at a no-go tone to avoid an air-puff punishment[7] (**Fig. 1a**). LC-NE neurons have crucial roles in this task: low phasic LC-NE activity pre-press facilitates task execution on low stimulus evidence trials, while high phasic LC-NE activity following an unexpected outcome, such as a false alarm followed by an air-puff or a correct rejection followed by a reward, mediates behavioral changes on the next trial several seconds later[7] (**Fig. 1b, c, d**). After a false alarm, the stimulus-response psychometric curve is shifted such that mice perform fewer false alarms and more hits on the next trial, resulting in a serial response bias which improves response sensitivity or d-prime on the subsequent trial (**Fig. 1c, d**). The increase in d-prime following a false alarm is also significantly higher than after hits or unreinforced (miss and correct rejection) trials (**Extended Data Fig. 1**). Thus, a phasic LC-NE signal following a surprising outcome facilitates behavioral performance on the next trial, several seconds later.

3

Importantly, the role of phasic LC-NE activity in this learned behavior is distinct from the role of tonic LC-NE activity in regulating arousal[7].

Due to their spatiotemporally diverse activity patterns and their proximity to ~100,000 synapses per astrocyte[31,32], we hypothesized that astrocytes could temporally expand phasic learning signals and alter neuronal population dynamics to improve performance after such a prediction error. Notably, astrocytes express α1 adrenergic (Adra1a) receptors and have been shown to be responsive to NE release during vigilance and internal states[33]. They have been suggested to mediate switches in cortical states in response to NE signaling[13], but whether they play a central role in learned behaviors remains unexplored. To examine astrocyte activity in response to controlled NE release *in vivo*, we first used 2-photon imaging of astrocyte calcium after optogenetic activation of channelrhodopsin (ChR2)-expressing NE axons through a cranial window in the visual cortex (**Extended Data Fig. 2a, b**). We found that astrocyte calcium increased nonlinearly with NE release in the cortex, such that longer stimulation paradigms elicited exponential-like increases in calcium responses (**Extended Data Fig. 2c**). Thus, cortical astrocytes are indeed responsive to NE release in vivo, with higher calcium elevations in response to larger NE release.

To examine the effects of NE on astrocytes and neurons in target regions during behavior, we used dual 2-photon imaging of astrocyte and neuronal calcium responses in the cortex of mice performing the go/no-go task (**Fig. 1e, f**). We have previously shown that prefrontal cortex and motor cortex are involved in the task and receive similar NE signals following a false alarm [7]. We found that motor cortex astrocytes were largely unresponsive during hit, miss, and correct rejection trials, but exhibited large, sustained increases in calcium activity following a false alarm air-puff (**Fig. 1g - i; Extended Data Fig. 2d, e**). We observed heterogeneity in astrocyte calcium responses to a false alarm (**Fig. 1h**), with some astrocytes exhibiting higher average and peak elevations in calcium than others (**Extended Data Fig. 2c - e**). Consistent with these findings, we found variable *Adra1a* mRNA expression in astrocytes in motor cortex slices, with some astrocytes expressing high levels of *Adra1a* mRNA and others low to none (**Extended Data Fig. 2f – h**). These results may also help explain the relatively nonlinear increase in astrocyte calcium responses after optogenetic activation of ChR2-expressing NE axons, whereby activation of astrocytes with low levels of *Adra1a* requires large NE transients.

4

Comparing astrocyte calcium increases with neuronal calcium increases during the task, we found that neuronal responses had faster rise times but smaller durations that were shorter than the inter-trial interval in our task (**Fig. 1j**), suggesting that persistent neuronal activity alone is not sufficient to bridge one trial and the next. Astrocyte calcium responses were significantly larger and remained elevated for significantly longer durations, spanning the inter-trial interval (**Fig. 1j – l**). Finally, while neurons exhibited heterogeneous activity during the task and were responsive to multiple trial types, astrocytes were almost exclusively activated in response to false alarm trials, with some activity on hit trials (**Fig. 1m; Extended Data Fig. 2i - k**). These data demonstrate that astrocytes are highly responsive to a surprising air-puff reinforcement following a false alarm, and have long-lasting calcium increases which could thus impact behavior over longer timescales than cortical neurons.

NE-astrocyte signaling mediates improvements in behavioral performance

To investigate whether astrocyte calcium increases following a false alarm were dependent on NE release, we measured astrocyte calcium responses in mice while reversibly chemogenetically silencing LC-NE neurons. We expressed a floxed Gi-coupled designer receptor exclusively activated by designer drugs (DREADD) in Dbh-Cre mice and imaged astrocyte calcium 30 minutes after injecting low-dose CNO or saline (**Fig. 2a, b**). When Gi-DREADDs in the LC were activated using CNO, astrocytes in the motor cortex were less responsive to a false alarm than during saline sessions, exhibiting lower magnitude peak and average responses and shorter duration of responses, suggesting that astrocyte calcium increases importantly reflect LC-NE signaling (**Fig. 2c, d; Extended Data Fig. 3a – c**). Because optogenetic silencing of LC-NE neurons prevents the behavioral gain of false alarm punishments on the next trial [7], these findings suggest that astrocyte calcium increases in response to phasic LC-NE release are causal for the behavior.

Since astrocytes could be responding to activity in nearby neurons following a false alarm, we next evaluated whether NE binding to adrenergic receptors on astrocytes is critical for the increase in calcium following a false alarm. Using *Adra1a fl/fl* mice, we expressed GFAP(0.7)-mCherry-T2A-iCre and GFAP-GCaMP6f in cortical astrocytes to selectively knock down Adra1a receptors in a subset of cortical astrocytes and imaged the calcium activity in the same astrocytes during the task (**Fig. 2e, f**). Without Adra1a receptors, cortical astrocytes no longer exhibited

increases in calcium following a false alarm, with calcium response magnitudes similar to other trial outcomes (**Fig. 2fg, h**). We compared astrocyte calcium responses in *Adra1a fl/fl* mice to mice with no manipulations and saw a significant decrease in false alarm response magnitude in the Adra1a receptor KD mice (**Extended Data Fig. 4a – c**). These data indicate that astrocytes respond directly to NE release post-false alarm via Adra1a receptors and not indirectly by reflecting the activity of nearby neurons.

We next asked whether the increase in astrocyte calcium following a false alarm is critical for the behavioral improvement observed after a false alarm. To manipulate astrocyte calcium dynamics, we expressed Gq-DREADD in astrocytes in the prefrontal and motor cortex of mice trained in the go/no-go task, and activated the DREADDs using i.p. injections of low-dose CNO 30 minutes prior to behavioral testing and imaging (**Fig. 2i**). Consistent with our previous findings, when we injected saline as control we saw dynamic astrocyte calcium activity over the course of the session, with large peaks in population activity largely correlating with false alarms (**Fig. 2j**). When we activated the DREADD however, astrocyte calcium activity no longer showed dynamic changes (**Fig. 2k**). Indeed, when we aligned calcium activity to the behavior, astrocyte calcium activity following a false alarm was highly attenuated (**Fig. 2l, m**) and showed a significant reduction in the mean response amplitude and duration compared with saline controls (**Fig. 2n, o**). We observed little effect on astrocyte calcium responses following hit, miss, and correct rejection trials, which all typically induce low levels of calcium activity (**Extended Data Fig. 5a – e**). Thus, Gq-DREADD activation was sufficient for studying the effects of blunting astrocyte calcium dynamics in our behavioral task. We next assessed the effects of astrocyte calcium manipulation via Gq-DREADD on serial response bias observed in the task. We found that in saline sessions, mice performed fewer false alarms and had improved response sensitivity or d-prime on trials after a false alarm, similar to wild-type animals, while in CNO sessions the same mice no longer exhibited this improvement in performance following a false alarm (**Fig. 2p; Extended Data Fig. 6**). Taken together, these data demonstrate that astrocyte calcium dynamics mediate the improvement in response sensitivity on post-false alarm trials.

Astrocytes mediate serial learning via purinergic signaling to neurons

Previous studies have shown that astrocytes can release ATP[34–38] in response to NE[39,40], and that ATP is converted to adenosine extracellularly where it binds to A1 receptors on

neurons[37,41–44]. We thus hypothesized that in our task, cortical astrocytes that are activated by NE following a false alarm could influence neuronal activity on the next trial via purinergic signaling.

To address this hypothesis, we first measured adenosine release in astrocyte cultures in response to NE using a fluorometric assay (**Fig. 3a**). Upon addition of NE, we saw a significant increase in adenosine fluorescence in the media. Blocking Adra1a receptors with the selective antagonist prazosin prevented the increase in adenosine fluorescence (**Fig. 3b**), suggesting that NE binding to Adra1a receptors on astrocytes can cause increases in extracellular adenosine.

We next asked whether mice trained in the reinforcement learning task show lasting changes in purinergic signaling pathways in cortical astrocytes. We examined the expression of 40 genes implicated in the ATP/adenosine pathway based on previous literature and the PANTHER and Reactome databases [40,45–48] and compared gene expression changes between trained mice and untrained control mice (untrained mice were water restricted for the same duration as trained mice). Motor and prefrontal cortex were extracted from these mice, astrocytes were isolated [49], and gene expression changes were measured by quantitative real-time PCR (qRT-PCR) (**Fig. 3c**). We assessed the purity of the isolated astrocytes by comparing the expression levels of different brain cell-type markers; samples from both groups were similarly enriched in astrocyte-specific genes (**Extended Data Fig. 7a**). Of the genes examined, 15 showed significant up- or down-regulation in trained mice, as expected for a complex signaling pathway; these included ATP synthases (*Atp5b, Atp5a1*), phosphodiesterase (*Pde4a*), IP3 receptors (*Itpr1, Itpr2*), ABC transporters (*Abcb1a, Abcb4*), nucleoside transporter (*Slc29a3*), beta-adrenergic receptor (*Adrb1*), adenosine receptors (*Adora2a, Adora2b*), and purinergic receptors (*P2rx3, P2rx4, P2ry12, P2ry13*) (**Fig. 3d; Extended Data Fig. 7b**). Annotating the genes to Gene Ontology (GO) terms showed the wide involvement of these genes in purinergic signaling, including ATP synthesis and transmembrane transport (**Fig. 3e**). Thus, training mice in the task alters the expression of genes that influence ATP signaling in astrocytes, and potentially from astrocytes to neurons.

We therefore asked whether the action of ATP/adenosine on neurons mediates behavioral improvement in our task, by assessing the effects of blocking neuronal adenosine A1 receptors in motor and prefrontal cortex *in vivo* in mice performing the task. When we applied DPCPX, a selective A1 receptor antagonist, topically to these cortical regions, mice no longer exhibited an increase in d-prime after a false alarm (**Fig. 3f; Extended Data Fig. 8**). Overall, our findings

7

suggest that purinergic signaling from astrocytes to neurons is critical for the behavioral improvement observed after an unexpected outcome in our task.

210

Astrocyte calcium manipulations and A1 receptor blockers reduce neuronal discriminability of stimuli post- false alarm

Finally, we asked how neuronal computations in cortex were influenced by a false alarm and subsequent air-puff in our task, and how manipulating astrocyte calcium increase and blocking astrocyte-neuron purinergic signaling in response to NE affected these computations. We hypothesized that the improved d-prime on trials after a false alarm could be due to improved neuronal discriminability of go and no-go stimuli on these trials. To address this hypothesis, we generated high density neuropixels recordings of neurons in the prefrontal cortex of mice performing the task. We recorded neurons from the same mice with either saline, CNO activation of Gq-DREADD in cortical astrocytes, or topical application of the A1 receptor antagonist DPCPX (**Fig. 4a**); using the same mice with enough wash-out between experiments importantly enabled direct comparison between manipulations. Focusing on the epoch after stimulus tone onset, we analyzed the difference in single-cell firing rates between go and no-go stimulus trials following specific trial outcomes. In saline sessions, we observed a clear firing rate difference between go and no-go stimuli after a false alarm, which was not apparent in CNO and DPCPX sessions (**Fig. 4b, c**). This difference in go/no-go firing rates following a false alarm was larger compared to other trial outcomes in saline sessions, but not in CNO and DPCPX sessions, or after other trial outcomes (**Fig. 4b - d**; **Extended Data Fig. 9a – c**). Thus, a post-false alarm air-puff elicited a specific increase in firing rate in response to stimuli on the following trial which did not occur when astrocyte calcium dynamics or A1 receptors were blocked. To quantify the discriminability of go vs no-go stimuli in neural responses, we computed the neural d-prime between responses to these stimuli to show firing rate differences in units of trial-to-trial variability. We found that in saline sessions, neural d-prime increased significantly following a false alarm compared to trials with no previous reinforcement, with both a multiplicative gain and a positive offset (**Fig. 4e**). Such an increase in stimulus discriminability after a false alarm was absent in CNO and DPCPX sessions. The overall neural d-prime after a false alarm was also significantly larger in saline sessions compared to CNO and DPCPX sessions (**Fig. 4f**). Our findings thus demonstrate that following a

false alarm, phasic NE release and subsequent astrocyte calcium and purinergic signaling alters neuronal responses to improve discriminability of go and no-go stimuli on the next trial (**Fig. 4g**).

240

Discussion

Using a behavioral task that causes LC-NE activation to facilitate serial, on-line learning, we demonstrate for the first time an instrumental role for astrocyte signaling in the implementation of such learning in the brain. We show that NE released transiently from the LC after an unexpected outcome acts directly on cortical astrocytes, which exhibit sustained increases in calcium, enabling a phasic NE learning signal to bridge across trials several seconds apart (**Fig. 1**). NE acts on astrocyte Adra1a receptors to increase intracellular calcium, and these calcium dynamics are necessary for the improved behavioral performance observed after a false alarm (**Fig. 2**). NE binding to astrocytic Adra1a receptors activates extracellular adenosine signaling *in vitro*, and trained mice exhibit changes in ATP/adenosine pathway genes expressed by astrocytes (**Fig. 3**). Adenosine binding to neuronal A1 receptors is necessary for behavioral performance improvement following an unexpected outcome (**Fig. 3**). After a false alarm, prefrontal cortex neurons exhibit improved discriminability between go and no-go stimuli on the following trial, and this improvement is occluded by manipulating astrocyte calcium or by blocking A1 receptors (**Fig. 4**). Taken together, our findings demonstrate that astrocytes integrate NE-mediated prediction errors and propagate these signals across trials to alter neuronal task encoding and influence behavioral performance.

Astrocytes are known to be responsive to multiple neurotransmitters and neuromodulators[10–12,25,40]. Our findings demonstrate the critical role of NE acting on astrocyte Adra1a receptors in eliciting large calcium increases during behavior, consistent with recent findings on NE influences on astrocyte signaling to regulate arousal[13]. GPCR coupled signaling to purinergic pathways in astrocytes has been described[40,41], and adenosine release has been shown to promote sleep[50] and act on A1 receptors on presynaptic terminals to inhibit excitatory transmission in slices[39,51,52]. In the context of *in vivo* brain circuits, however, adenosine would be expected to have more complex effects, by inhibiting excitatory transmission to both excitatory and inhibitory neurons, affecting inhibitory transmission directly and indirectly[52,53], as well as activating adenosine A2 receptors on astrocytes themselves[54]. Coupled with the contact of individual astrocytes with massive numbers of synapses[32], it is reasonable to propose that

9

270 astrocytes exert coordinated task-specific influences on large populations of neurons. Thus, as we demonstrate, they alter task encoding by neuronal populations, and by their activation critically bridge NE signaling, neuronal dynamics, and behavioral outcome.

Astrocytes have been implicated in a range of behaviors[11,12,55], but their has been largely viewed as modulatory, emphasizing their role in shaping glutamatergic transmission[56], GABAergic transmission[53], and local neurotransmitter sensing[57]. In contrast, our findings now demonstrate that

275 cortical astrocytes are directly activated by NE and play an essential, instrumental role in signaling prediction error to alter neuronal responses and shape behavior. What could be the evolutionary and computational advantage of having cells such as astrocytes, with long time scales of calcium and purinergic signaling, built so deeply into the propagation of prediction errors? Extrapolating from our task, we suggest that to optimize behavior these signals need to last sufficiently long to

280 be available at the time when they are needed to influence subsequent behavior. Thus astrocytes may be crucial more generally for constructing and refining internal models of the world - a fundamental component of cognition – at time scales consequential for natural behavior.

References

285 1. Lee, D., Seo, H. & Jung, M. W. Neural Basis of Reinforcement Learning and Decision Making. *Annu. Rev. Neurosci.* **35**, 287–308 (2012).

2. Dayan, P. & Niv, Y. Reinforcement learning: the good, the bad and the ugly. *Curr. Opin. Neurobiol.* **18**, 185–196 (2008).

3. Dayan, P. & Daw, N. D. Decision theory, reinforcement learning, and the brain. *Cogn. Affect.*
290 *Behav. Neurosci.* **8**, 429–453 (2008).

4. Aston-Jones, G. & Cohen, J. D. An integrative theory of locus coeruleus-norepinephrine function: adaptive gain and optimal performance. *Annu. Rev. Neurosci.* **28**, 403–450 (2005).

5. Sara, S. J. The locus coeruleus and noradrenergic modulation of cognition. *Nat. Rev. Neurosci.* **10**, 211–223 (2009).

295 6. Jordan, R. The locus coeruleus as a global model failure system. *Trends Neurosci.* **47**, 92–105 (2024).

7. Breton-Provencher, V., Drummond, G. T., Feng, J., Li, Y. & Sur, M. Spatiotemporal dynamics of noradrenaline during learned behaviour. *Nature* **606**, 732–738 (2022).

8. Clarke, L. E. & Barres, B. A. Emerging roles of astrocytes in neural circuit development.
300 *Nat. Rev. Neurosci.* **14**, 311–321 (2013).

9. Perea, G., Sur, M. & Araque, A. Neuron-glia networks: integral gear of brain function. *Front. Cell. Neurosci.* **8**, 378 (2014).

10. Verkhratsky, A. & Nedergaard, M. Physiology of Astroglia. *Physiol. Rev.* **98**, 239–389 (2018).

305 11. Nagai, J. *et al.* Behaviorally consequential astrocytic regulation of neural circuits. *Neuron* **109**, 576–596 (2021).

12. Kofuji, P. & Araque, A. Astrocytes and Behavior. *Annu. Rev. Neurosci.* **44**, 49–67 (2021).

11

13. Reitman, M. E. *et al.* Norepinephrine links astrocytic activity to regulation of cortical state. *Nat. Neurosci.* 1–15 (2023) doi:10.1038/s41593-023-01284-w.

310   14. Mu, Y. *et al.* Glia Accumulate Evidence that Actions Are Futile and Suppress Unsuccessful Behavior. *Cell* **178**, 27-43.e19 (2019).

15. Rasmussen, R. N., Asiminas, A., Carlsen, E. M. M., Kjaerby, C. & Smith, N. A. Astrocytes: integrators of arousal state and sensory context. *Trends Neurosci.* **46**, 418–425 (2023).

16. Ma, Z., Stork, T., Bergles, D. E. & Freeman, M. R. Neuromodulators signal through
315   astrocytes to alter neural circuit activity and behaviour. *Nature* **539**, 428–432 (2016).

17. Bekar, L. K., He, W. & Nedergaard, M. Locus Coeruleus α-Adrenergic–Mediated Activation of Cortical Astrocytes In Vivo. *Cereb. Cortex N. Y. NY* **18**, 2789–2795 (2008).

18. Ding, F. *et al.* α1-Adrenergic receptors mediate coordinated Ca2+ signaling of cortical astrocytes in awake, behaving mice. *Cell Calcium* **54**, 387–394 (2013).

320   19. Paukert, M. *et al.* Norepinephrine Controls Astroglial Responsiveness to Local Circuit Activity. *Neuron* **82**, 1263–1270 (2014).

20. Slezak, M. *et al.* Distinct Mechanisms for Visual and Motor-Related Astrocyte Responses in Mouse Visual Cortex. *Curr. Biol. CB* **29**, 3120-3127.e5 (2019).

21. Stobart, J. L. *et al.* Cortical Circuit Activity Evokes Rapid Astrocyte Calcium Signals on a
325   Similar Timescale to Neurons. *Neuron* **98**, 726-735.e4 (2018).

22. Wang, X. *et al.* Astrocytic Ca2+ signaling evoked by sensory stimulation in vivo. *Nat. Neurosci.* **9**, 816–823 (2006).

23. Winship, I. R., Plaa, N. & Murphy, T. H. Rapid astrocyte calcium signals correlate with neuronal activity and onset of the hemodynamic response in vivo. *J. Neurosci. Off. J. Soc.*
330   *Neurosci.* **27**, 6268–6272 (2007).

24. Schummers, J., Yu, H. & Sur, M. Tuned responses of astrocytes and their influence on hemodynamic signals in the visual cortex. *Science* **320**, 1638–1643 (2008).

25. Khakh, B. S. & Sofroniew, M. V. Diversity of astrocyte functions and phenotypes in neural circuits. *Nat. Neurosci.* **18**, 942–952 (2015).

26. Bouret, S. & Sara, S. J. Reward expectation, orientation of attention and locus coeruleus-medial frontal cortex interplay during learning. *Eur. J. Neurosci.* **20**, 791–802 (2004).

27. Vazey, E. M., Moorman, D. E. & Aston-Jones, G. Phasic locus coeruleus activity regulates cortical encoding of salience information. *Proc. Natl. Acad. Sci.* **115**, E9439–E9448 (2018).

28. Bari, A. *et al.* Differential attentional control mechanisms by two distinct noradrenergic coeruleo-frontal cortical pathways. *Proc. Natl. Acad. Sci.* **117**, 29080–29089 (2020).

29. Breton-Provencher, V., Drummond, G. T. & Sur, M. Locus Coeruleus Norepinephrine in Learned Behavior: Anatomical Modularity and Spatiotemporal Integration in Targets. *Front. Neural Circuits* **15**, (2021).

30. Jordan, R. & Keller, G. B. The locus coeruleus broadcasts prediction errors across the cortex to promote sensorimotor plasticity. *eLife* **12**, RP85111 (2023).

31. Bushong, E. A., Martone, M. E., Jones, Y. Z. & Ellisman, M. H. Protoplasmic astrocytes in CA1 stratum radiatum occupy separate anatomical domains. *J. Neurosci. Off. J. Soc. Neurosci.* **22**, 183–192 (2002).

32. Allen, N. J. & Eroglu, C. Cell Biology of Astrocyte-Synapse Interactions. *Neuron* **96**, 697–708 (2017).

33. Oe, Y. *et al.* Distinct temporal integration of noradrenaline signaling by astrocytic second messengers during vigilance. *Nat. Commun.* **11**, 471 (2020).

34. Gordon, G. R. J. *et al.* Norepinephrine triggers release of glial ATP to increase postsynaptic efficacy. *Nat. Neurosci.* **8**, 1078–1086 (2005).

355 35. Broadhead, M. J. & Miles, G. B. Bi-Directional Communication Between Neurons and Astrocytes Modulates Spinal Motor Circuits. *Front. Cell. Neurosci.* **14**, (2020).

36. Gourine, A. V. *et al.* Astrocytes Control Breathing Through pH-Dependent Release of ATP. *Science* **329**, 571–575 (2010).

37. Pascual, O. *et al.* Astrocytic Purinergic Signaling Coordinates Synaptic Networks. *Science*

360 **310**, 113–116 (2005).

38. Shen, W., Nikolic, L., Meunier, C., Pfrieger, F. & Audinat, E. An autocrine purinergic signaling controls astrocyte-induced neuronal excitation. *Sci. Rep.* **7**, 11280 (2017).

39. Lefton, K. B. *et al.* Norepinephrine Signals Through Astrocytes To Modulate Synapses. Preprint at https://doi.org/10.1101/2024.05.21.595135 (2024).

365 40. Kofuji, P. & Araque, A. G-Protein-Coupled Receptors in Astrocyte-Neuron Communication. *Neuroscience* **456**, 71–84 (2021).

41. Lezmy, J. How astrocytic ATP shapes neuronal activity and brain circuits. *Curr. Opin. Neurobiol.* **79**, 102685 (2023).

42. Andersson, M., Blomstrand, F. & Hanse, E. Astrocytes play a critical role in transient

370 heterosynaptic depression in the rat hippocampal CA1 region. *J. Physiol.* **585**, 843–852 (2007).

43. Chen, J. *et al.* Heterosynaptic long-term depression mediated by ATP released from astrocytes. *Glia* **61**, 178–191 (2013).

44. Serrano, A., Haddjeri, N., Lacaille, J.-C. & Robitaille, R. GABAergic Network Activation of Glial Cells Underlies Hippocampal Heterosynaptic Depression. *J. Neurosci.* **26**, 5370–5382 (2006).

45. Sheth, S., Brito, R., Mukherjea, D., Rybak, L. P. & Ramkumar, V. Adenosine receptors: expression, function and regulation. *Int. J. Mol. Sci.* **15**, 2024–2052 (2014).

46. Sumi, Y. *et al.* Adrenergic receptor activation involves ATP release and feedback through purinergic receptors. *Am. J. Physiol. - Cell Physiol.* **299**, C1118–C1126 (2010).

47. Burnstock, G. Physiology and Pathophysiology of Purinergic Neurotransmission. *Physiol. Rev.* **87**, 659–797 (2007).

48. Bodin, P. & Burnstock, G. Purinergic Signalling: ATP Release. *Neurochem. Res.* **26**, 959–969 (2001).

49. Holt, L. M. & Olsen, M. L. Novel Applications of Magnetic Cell Sorting to Analyze Cell-Type Specific Gene and Protein Expression in the Central Nervous System. *PLOS ONE* **11**, e0150290 (2016).

50. Halassa, M. M. *et al.* Astrocytic modulation of sleep homeostasis and cognitive consequences of sleep loss. *Neuron* **61**, 213–219 (2009).

51. Corkrum, M. *et al.* Dopamine-Evoked Synaptic Regulation in the Nucleus Accumbens Requires Astrocyte Activity. *Neuron* **105**, 1036-1047.e5 (2020).

52. Boddum, K. *et al.* Astrocytic GABA transporter activity modulates excitatory neurotransmission. *Nat. Commun.* **7**, 13572 (2016).

53. Matos, M. *et al.* Astrocytes detect and upregulate transmission at inhibitory synapses of somatostatin interneurons onto pyramidal cells. *Nat. Commun.* **9**, 4254 (2018).

15

54. Theparambil, S. M. *et al.* Adenosine signalling to astrocytes coordinates brain metabolism and function. *Nature* 1–8 (2024) doi:10.1038/s41586-024-07611-w.

55. Murphy-Royal, C., Ching, S. & Papouin, T. A conceptual framework for astrocyte function. *Nat. Neurosci.* 1–9 (2023) doi:10.1038/s41593-023-01448-8.

56. Delepine, C., Shih, J., Li, K., Gaudeaux, P. & Sur, M. Differential Effects of Astrocyte Manipulations on Learned Motor Behavior and Neuronal Ensembles in the Motor Cortex. *J. Neurosci.* **43**, 2696–2713 (2023).

57. Cahill, M. K. *et al.* Network-level encoding of local neurotransmitters in cortical astrocytes. *Nature* **629**, 146–153 (2024).

58. Shamash, P., Carandini, M., Harris, K. & Steinmetz, N. A tool for analyzing electrode tracks from slice histology. 447995 Preprint at https://doi.org/10.1101/447995 (2018).

59. Kim, J., Rahman, M. H., Lee, W. H. & Suk, K. Chemogenetic stimulation of the Gi pathway in astrocytes suppresses neuroinflammation. *Pharmacol. Res. Perspect.* **9**, e00822 (2021).

60. Vaidyanathan, T. V., Collard, M., Yokoyama, S., Reitman, M. E. & Poskanzer, K. E. Cortical astrocytes independently regulate sleep depth and duration via separate GPCR pathways. *eLife* **10**, e63329 (2021).

61. Bankhead, P. *et al.* QuPath: Open source software for digital pathology image analysis. *Sci. Rep.* **7**, 16878 (2017).

Materials and Methods

Mice

All procedures performed in this study were in accordance with the Massachusetts Institute of Technology's Animal Care and Use Committee and the Guide for the Care and Use of Laboratory Animals published by the National Institutes of Health. Male and female mice more than 2 months old were used in this study. Mice were kept in a room with a (12:12) reversed light/dark cycle with controlled temperature and ventilation (20–22 °C; 40–60% humidity). All experiments were performed during the dark period of the cycle. The Dbh-cre line (Jackson Laboratories) was used for specific expression of Gi-DREADD virus in norepinephrine-expressing neurons of the locus coeruleus (LC). The *Adra1a^{fl/fl}* line (University of California San Francisco) was used for astrocyte-specific Adra1a knock-down experiments. C57BL/6 wild-type mice (Jackson Laboratories) were used for all other experiments.

Viral vectors

For dual imaging of cytosolic astrocyte calcium activity and neuronal calcium activity, wild type mice were injected with AAV5-GFAP-cyto-GCaMP6 (Addgene #52925-AAV5) and AAV1-Syn-NES-jRGECO1a-WPRE (Addgene #100854-AAV1) into motor cortex (MC). For chemogenetic manipulation of astrocytes, wild type mice were injected with AAV5-GFAP-hM3D(Gq)-mCherry (Addgene #50478-AAV5) into motor cortex (MC) and prefrontal cortex (PFC). For chemogenetic silencing of the LC while imaging in the MC, Dbh-Cre mice were injected with AAV5-hSyn-DIO-hM4D(Gi)-mCherry (Addgene #44362-AAV5) into the LC and AAV5-GFAP-cyto-GCaMP6 (Addgene #52925-AAV5) into the MC. For Adra1a knock-down experiments while imaging in the MC, *Adra1a^{fl/fl}* mice were injected with AAV5-GFAP(0.7)-mCherry-T2A-iCre (Vector Biolabs #VB1132) and AAV5-GFAP-cyto-GCaMP6 (Addgene #52925-AAV5) into the MC. For LC axonal stimulation, Dbh-Cre mice were injected with AAV1-EF1a-double floxed-hChR2(H134R)-EYFP (Addgene #20298-AAV1) in the LC and AAV5-GFAP-cyto-GCaMP6 (Addgene #52925-AAV5) into the visual cortex.

Stereotactic surgery

Surgeries were performed aseptically under isoflurane anesthesia while maintaining body temperature at 37.5°C on a heating pad (ATC2000, World Precision Instruments). Mice were given pre-operative slow-release buprenorphine (1mg/kg, subcutaneous injection) as well as pre- and post-operative meloxicam (5mg/kg, subcutaneous injection). Mice were placed in a stereotaxic frame (model 51725D, Stoelting), scalp hair was removed with a depilatory cream, and the incision site was sterilized using betadine and 70% ethanol. The skull was exposed and the conjunctive tissue was removed using hydrogen peroxide. The skull was positioned such that the bregma and lambda marks were aligned on the anteroposterior and dorsoventral axes. For virus delivery, a small craniotomy (0.5 mm) was drilled above the region of interest and virus was injected using a glass pipette with a 50 µm diameter tip. For delivering Gi-DREADD virus to the LC, 300 nl of virus was injected (rate: 50nl/min). Coordinates for targeting the LC were (in mm): -5.2 to -5.0 anterior-posterior (AP), ±0.9 medial-lateral (ML), -2.8 dorsal-ventral (DV). For delivering Gq-DREADD virus to the cortex, 200 nl of virus was injected (rate: 50nl/min) into the motor cortex (MC) and prefrontal cortex (PFC) bilaterally. Coordinates for targeting the PFC were (in mm): +2.0 AP, ± 0.3 ML, -0.5 DV. Coordinates for targeting the MC were (in mm): +0.5 AP, ±1.5 ML, -0.3 DV. For 2-photon calcium imaging, a round 3 mm diameter craniotomy was drilled over the

left MC. Three to four injections of 250nl of virus were made into layer 2/3 of the MC (DV - 0.3mm, rate: 50nl/min), waiting 5 minutes before withdrawing the glass pipette after each injection to avoid backflow. A cranial window, made of two 3 mm coverslips centered on a 5 mm coverslip (CS-3R, CS-5R; Warner Instruments) and glued together with ultraviolet adhesive, was positioned
465   over the craniotomy and attached to the skull using dental cement (C&B Metabond, Parkell). To avoid light reflection and absorption, the dental cement was mixed with black ink pigment (Black Iron Oxide 18727, Schmincke). A head plate was then affixed to the skull with dental cement for head fixation during the behavioral task. Following surgery, animals were allowed to recover on a heating pad. Their recovery was monitored for a minimum of 72 hours and anti-inflammatory
470   (Meloxicam) injections were provided as needed. Animals recovered for at least 5 days before starting water restriction for behavioral experiments.

Behavior set-up
Mice were head-fixed on a behavior rig and confined in a polypropylene tube to limit body
475   movements. Their left forepaw was able to move a lever built with a 1/16-mm-thick brass rod attached to a piezoelectric flexible force transducer (LCL-005, Omega Engineering), and a metallic lick spout placed near the mouse's mouth and connected to a custom-made 80 lick detector was used to deliver water rewards (~5 μL drop of water). A small tube, pointing towards the mouse's facial area and at a distance of 3 cm, was used to deliver air puff punishment (compressed air at
480   40 psi for 0.3s). Voltage signals from the transducer were recorded through a microcontroller board (Arduino UNO Rev3). Voltage signal from the transducer was converted to lever movement in degrees using calibration data from video analysis. A second microcontroller board was used to control a 5 mm yellow LED light placed 8 cm if front of the mouse and two solenoid valves (Parker #003-0141-900) for water and air puff delivery. 4 or 12 kHz sound stimuli of 0.5s duration were
485   delivered using a single speaker located at a distance of 30 cm from the mouse. The speaker frequency range was calibrated using a USB calibrated measurement microphone (UMIK-1, Mini DSP) and the Room EQ Wizard software, and the sound stimulus intensities were established by a sound level meter. Two behavior rigs were used: one for general behavior and electrophysiology, and one for 2-photon imaging. Noise levels were comparable across both rigs (in dB with Z noise
490   frequency weightings): 7.8±1.1, 8.8±1.0, 14.3±0.8, and 14.7±0.9 for 4 kHz; and -4.0±1.2, -1.7±1.1, -1.9±0.9, and 0.3±0.7 for 12 kHz. The behavior rig was connected to a computer running a custom written MATLAB (Mathworks) script that was able to record lever voltage, while controlling the timing of light cue, sound (using Psychtoolbox), water, and reward. Behavior rigs were assembled primarily with optomechanical components (Thorlabs).
495

Behavior task
Upon recovery from surgical procedure, mice were gradually put on a water restriction schedule, eventually receiving 1-1.5 mL of water per day. Body weight was maintained above 90% of their pre-restriction weight. Mice were trained to hold still for 1s during the cue period (LED on), to
500   wait for a delay to hear a tone, and to either push the lever to obtain a reward or to refrain from pushing to avoid a punishment. Mice learned to push the lever when they heard a go tone (12 kHz frequency) and hold still when they heard a no-go tone (4 kHz). After the onset of the 0.5s sound stimulus, mice had 0.8s to respond or hold still. If they pressed the lever during a go trial, they received a water reward. If they pressed during a no-go trial, they received a mild air puff
505   punishment. Absence of response on go trials (miss) or not pressing the lever during no-go trials (correct rejections) were not reinforced. To vary the level of stimulus evidence, 4 intensities were

used per frequency for a total of 8 different stimuli. Tone intensities used were 5, 15, 25, and 35 dB. These values were calculated by measuring the sound pressure level for either go or no-go frequency and subtracting the noise level of that given frequency. A lever press (hit or false alarm) was determined when the lever position reached a threshold value of 3 to 4° (depending on the animal) from the position at the beginning of the trial, while absence of a lever press (miss or correct rejection) was determined if the lever absolute position stayed below a value of 2.2°. Premature lever presses, which occurred in the delay period between light cue off and tone onset, were considered early presses and aborted the trial. The delay between light cue off and tone onset was randomized following a gaussian distribution (mean: 0.65s; standard deviation: 0.15s). Trial order was pseudo-randomized to ensure that the same amount of go or no-go trials were presented every fourth trial, and that each tone intensity was presented every eighth trial. Each trial was followed by a 4s-long intertrial interval (ITI). Mice were taken through two stages of training until they became proficient at the task. During the first phase of training, mice learned to associate a lever press with reward and to detect a go tone. In this phase, only go tones (tone: 12 kHz at 35 dB for 0.5s) were used. The same trial sequence as in the full task was used, but with an extended duration of the response window (30s instead of 0.8s). The animal was switched to the next stage once they made more than 80% of lever presses for 50 consecutive trials within a period of 0.8s after tone onset. During the second phase of training, no-go trials (tone: 4 kHz at 35 dB for 0.5s) were introduced and the response window was reduced to 0.8s after tone onset. Training in the second phase lasted until mouse performance reached 85% hit rate and less than 30% false alarm rate for two consecutive sessions. The last stage was considered the full task, in which 4 intensities of each tone were introduced (5, 15, 25, and 35 dB). For physiological recordings, a 0.25s delay between the timing of lever press and reward/punishment was introduced at the last stage.

2-photon calcium imaging

After training to proficiency, awake mice that were previously implanted with a cranial window were head-fixed, and the fluorescent sensors (GCaMP, jRGECO, and mCherry) were imaged using galvo-galvo scanning with a Prairie Ultima IV two-photon microscopy system (Bruker). Two-photon excitation was provided by an insight tunable laser (InSight X3+ or MaiTai, Spectra-Physics). Imaging of GCaMP was done at a wavelength of 920 nm, imaging of mCherry was done at 1020 nm, and dual-imaging of GCaMP and jRGECO was done at 1000 nm. A 16x 0.8 numerical aperture objective (Nikon) and 2-4x optical zoom was used for imaging, with a frame rate of 5-6 Hz. A voltage signal indicating the start of each trial was recorded by the system for alignment with the behavior (Bruker). Imaging sessions lasted ~25 minutes per animal.

LC axonal stimulation

Awake mice that were previously implanted with a cranial window were headfixed and ChR2 expressing axons were stimulated via a 473 nm laser through the objective for 0.5 – 2 seconds at 30 Hz. During stimulation, the shutter was closed and no images were captured.

Neuropixels recordings

After training to proficiency, mice that were previously injected with Gq-DREADD virus were anesthetized with isoflurane. The silicone elastomer and gel foam (Pfizer) covering the skull were removed and a 500-um diameter craniotomy was performed over the MC (+0.5 mm AP; +-1.5 mm ML) and PFC (+2 mm AP; +-0.3 mm ML). The dura was punctured and the craniotomy was protected with saline and a piece of gel foam (Pfizer). The skull was covered again with silicone

19

elastomer and the mouse was allowed to recover for one day before recording. The next day, the awake animal was head-fixed and the silicone elastomer and gel foam were gently removed. A 0.9% NaCl solution was used to keep the surface of the brain wet for the duration of recordings. After placing the animal on the recording set up, a reference silver wire was submerged in the saline solution on the skull surface. The neuropixels probe was then referenced on bregma and the surface of the brain. The probe was slowly lowered (1 min per mm) using a motorized micromanipulator (MP-285, Sutter Instrument Company) until the desired depth (~2000 µm) was reached. The probe was left to sit in the brain for at least 15 minutes prior to initiating the recording to minimize probe drift during the recording. Time stamps of each trial start were recorded by the neuropixels Spike GLX software. Physiology data was collected at a rate of 30 kHz using the Spike GLX software. Spike sorting was done using kilosort, and spikes were manually curated using Phy to remove artifacts picked by the algorithm such as ill-shaped units, units with low amplitude spikes, units with low spike rate, or units without a clear refractory period. Spike times were verified with cross correlograms to combine units or eliminate duplicates. For each unit, parts of the recordings with obvious drift (unit firing rate abruptly decreasing) were excluded. At the end of each session, the probe was coated with DiI, DiO, or DiD and reinserted at the same location and depth to mark the recording track. The craniotomy was covered again with gel-foam and silicone elastomer to allow recording on the next day. After the last recording, the brain was collected (see methods for histology) and imaged on a confocal microscope (Leica SP8). Slices with DiI, DiO, or DiD probe tracks were aligned to the Allen Brain Atlas using SHARP-Track [58] to verify the position of the probe.

Saline/CNO behavior

Clozapine-N-oxide dihydrochloride (CNO; Hello Bio) was dissolved in saline injectable sterile solution (0.9% sodium chloride) and administered at a low concentration of 0.2 mg/kg [59,60]. The CNO solution or saline control was injected intraperitoneally 30 minutes before each behavior session.

Saline/DPCPX behavior

8-cyclopentyl-1,3-dipropylxanthine (DPCPX; MilliporeSigma) was dissolved in DMSO and saline, and administered at a concentration of 10 µM[52]. Gel foam soaked in the 10 µM DPCPX solution or saline control was applied directly on the skull of a head-fixed animal that previously underwent craniotomies on the MC and PFC (see methods for neuropixels recording). The behavior session was started 15 minutes after initial DPCPX or saline application, allowing time for the solution to penetrate through the previously-punctured dura.

In situ hybridization

Mice were deeply anesthetized with isoflurane and transcardially perfused with cold 0.1 M phosphate buffered saline. The brain was then rapidly dissected and flash frozen in a cryomold held above liquid nitrogen. The frozen tissue was embedded in Tissue-Tek OCT compound (Sakura Finetek) prior to slicing on a cryostat (Leica CM 3050S). 14 µm sagittal sections were mounted directly on SuperFrost Plus slides (VWR) and stored at -80°C. Fluorescence in situ hybridization was conducted using the manufacturer's recommended protocol and reagents (RNAscope Multiplex Fluorescent V2 Assay, Advanced Cell Diagnostics). *Aqp4* and *Adra1a* were probed (417161-C4 and 408661, Advanced Cell Diagnostics) and labeled using 1:1500 diluted Opal 570 and 690 dyes respectively (Akoya Biosciences). Labeled sections were stained with DAPI,

600 mounted with Prolong Gold Antifade mounting media (ThermoFisher Scientific), and imaged on a confocal microscope (Leica SP8) using a 20x objective. Images were analyzed using QuPath software [61]. Cells were segmented based on nuclei staining by DAPI and cellular regions of interest (ROI) were defined 5µm around the nuclei. Within each ROI, the subcellular detection feature was used to quantify the number of mRNA puncta of each probe within the cell. Threshold values for optimal detection of each probe were set and remained unchanged for all images.

605

Histology

Mice were deeply anesthetized and transcardially perfused with cold 0.1 M phosphate buffered saline followed by 4% paraformaldehyde (PFA). Brains were collected and post-fixed in 4% PFA overnight at 4°C. Brains were then sectioned into 100 µm coronal sections with a vibratome (Leica
610 VT 1200S). Sections were mounted with Vectashield mounting media (Vector Laboratories) and imaged with a confocal microscope (Leica SP8) using a 10x objective to confirm viral expression in target regions.

Glial cell culture and adenosine assay

615 Brains of two-day-old neonatal C57BL/6 mice were removed after decapitation and cortices were dissected out using a dissecting microscope. The tissue was dissociated to a single cell suspension using enzymatic and mechanical trituration. The collected cell suspension was cultured in 35 mm culture dishes in Astrocyte medium (ScienCell) containing 10% fetal bovine serum and was maintained at 37°C in a humidified atmosphere containing 5% CO_2. The medium was changed
620 every 3–4 days. Cultures were used for the adenosine assay after 14 days. For the adenosine assay, the cell medium was replaced with physiological saline containing 120 mM NaCl, 4 mM KCl, 1.2 mM $MgSO_4$, 10 mM glucose, 2 mM $CaCl_2$, 10 mM HEPES, pH 7.35. During the experiment, cells were incubated with 20 µM NE for 5 min and an aliquot of saline was used to measure adenosine using an adenosine assay kit (Abcam) and a microplate reader (Perkin Elmer Enspire) after 30 min.
625 For evaluating effects of alpha1 adrenergic receptor inhibition, cells were pre-incubated in saline containing 10 µM prazosin hydrochloride (Sigma) for at least two hours before NE treatment.

Quantitative RT-PCR

Mice were deeply anesthetized under isoflurane and decapitated for rapid brain extraction. MC
630 and PFC from individual hemispheres were dissected in ice-cold ACSF containing the following (in mM): NaCl 125, KCl 3, $CaCl_2$ 2.5, $MgSO_4$ 1.3, NaH_2PO_4 1.25, $NaHCO_3$ 26, and glucose 13 bubbled with oxygen. Cells were dissociated using Neural Tissue Dissociation Kit–Postnatal Neurons (catalog #130-094-802, Miltenyi Biotec) and gentleMACS Dissociator following manufacturer protocols. Cell suspensions were depleted of microglia and myelin debris (Myelin
635 Removal Kit, catalog #130096733, Miltenyi Biotec), then astrocytes were isolated using the anti-ACSA-2 magnetic cell sorting kit and protocol (catalog #130097678, Miltenyi Biotec). RNA was purified and concentrated with proteinase K cell digestion, ethanol precipitation, and washing on a silica column (RNeasy mini kit, Qiagen). Total RNA samples were reverse transcribed (SuperScript VILO, ThermoFisher Scientific). qRT-PCR was perfomed using a QuantStudio 3
640 System (ThermoFisher Scientific) with TB Green Master Mix (Takara). The list of primers used is shown in Extended Data Table 1. Every sample was run in technical duplicate or triplicate. Relative expression was quantified using the ΔΔCq method with *Gapdh* as the endogenous control.

Behavioral analyses

21

645 For each animal, the average press probability for each stimulus tone was computed and averaged it across no-go and go tones to determine the false alarm rate (F) and hit rate (H), respectively. Behavioral stimulus discriminability was then quantified by calculating the d-prime (d') as follows:

650
$$d' = Z(H) - Z(F)$$

where Z represents the z-score. We calculated H, F, and d' after specific trial outcomes and on surrogate data generated by shuffling the trial sequence (N=1,000 shuffles). We then subtracted the average shuffled H, F, and d' from the values computed after a specific outcome to evaluate
655 the effect of specific previous outcomes on these metrics, compared to their values computed irrespective of the previous trial outcome. We excluded parts of a session where the hit rate was lower than 40% and false alarm rate was higher than 50%, calculated using a 50-trial averaging window.

660 *Imaging data analysis*
Time-lapse imaging sequences were corrected for x and y movement using the template-matching ImageJ plugin. For neuronal analysis, regions of interests (ROI) were automatically identified using Suite2P, manually curated, and the fluorescence intensity in time for each ROI was averaged. For astrocyte analysis, ROIs were manually drawn using ImageJ's ROI manager tool, and
665 fluorescence intensity over time was measured with ImageJ's multi-measure feature. Baseline fluorescence F_0 was computed as the average raw fluorescence of each cell over the entire recording session. Deviations from the baseline ΔF were computed as the raw fluorescence value at each time point minus F_0, divided by F_0. We quantified the mean activity and response timescale of each cell for specific trial types (hit, miss, correct rejection, and false alarm). Peak activity was
670 calculated as the maximum $\frac{\Delta F}{F_0}$ from 0 to 5 seconds after tone onset. To quantify response duration, we first identified time points at which the mean activity of each cell across specific trial types deviated positively or negatively from 0 by more than one standard deviation of the baseline activity variability (from -1 to -0.2 seconds from tone onset), computed across all trials. We then clustered consecutive threshold-exceeding time points (separately for positive and negative
675 deviations) within 10 seconds following tone onset, defining responsive cells as those with at least one activity cluster. The response timescale of each responsive cell was quantified as the duration of the longest activity cluster.

Neuropixels data analysis
680 For each neuron, we calculated the mean and standard deviation of the firing rate in sliding windows 50 ms long computed either over go or over no-go stimulus presentations, selecting trials after specific trial outcomes. The neural d' (a measure of go vs no-go discriminability based on the activity of an individual neuron) in each time window was then computed as follows:

685
$$neural\ d' = \frac{\mu_{go} - \mu_{no-go}}{\sqrt{\frac{1}{2}(\sigma_{go} - \sigma_{no-go})}}$$

We set neural d' values to zero in rare cases when a neuron did not fire any spike across all trials to both go and no-go stimuli. We also excluded the rare cases when the neuron fired some spikes

22

690   but with no variation of firing rate across-trials within both go and no-go conditions. For comparisons of neural d-prime across experimental conditions or following different trial outcomes within the same condition, we used the average d-prime value calculated from 0 to 500 ms from tone onset. To evaluate whether the neural d' after a punishment differed from the d' after no reinforcement in different experimental conditions, we performed a linear regression of the neural d' after a false alarm trial against the neural d' after a no reinforcement trial. To compute

695   the error of the regression slope coefficient, we performed bootstrap with resampling across cells (N = 20,000 bootstrap iterations) and repeated the regression for each bootstrap instantiation. The significance of the slope coefficient was estimated empirically by comparing the bootstrap distributions of slope values to 1 (two-tailed tests).

700   *Statistics*
Throughout the paper we used Student's t-statistics to compute P values of paired and unpaired comparisons. We used two-tailed tests, except for d-prime comparisons after a false alarm compared to after other trial outcomes in Gq-DREADD expressing and DPCPX treated animals, for which we used one-tailed tests to determine whether there was a specific behavioral

705   improvement after a false alarm. For Adra1a receptor KD experiments, we used a one-way ANOVA to compare astrocyte responses across trial types. To calculate 95% confidence interval of post-false alarm against post-unreinforced neural d-prime linear regression parameters we used bootstrap with resampling (n = 20,000 repetitions).

710

23

Author contributions:

Conceptualization: GTD, JS, MS; Methodology: GTD, AN, MC, JS, PO, YO, PCS, SP, MS; Investigation: GTD, AN, JS, PO, JP, GOS, KRJ, VB-P, PCS; Visualization: GTD, MC, PO; Funding acquisition: MS, SP; Supervision: MS, SP; Writing – original draft: GTD, MS; Writing – review & editing: GTD, AN, MC, KRJ, MS, SP.

Competing interests: The authors declare that they have no competing interests.

Data and materials availability: All data, code, and materials used in the analysis will be made available upon acceptance of the manuscript.

24

Figure 1
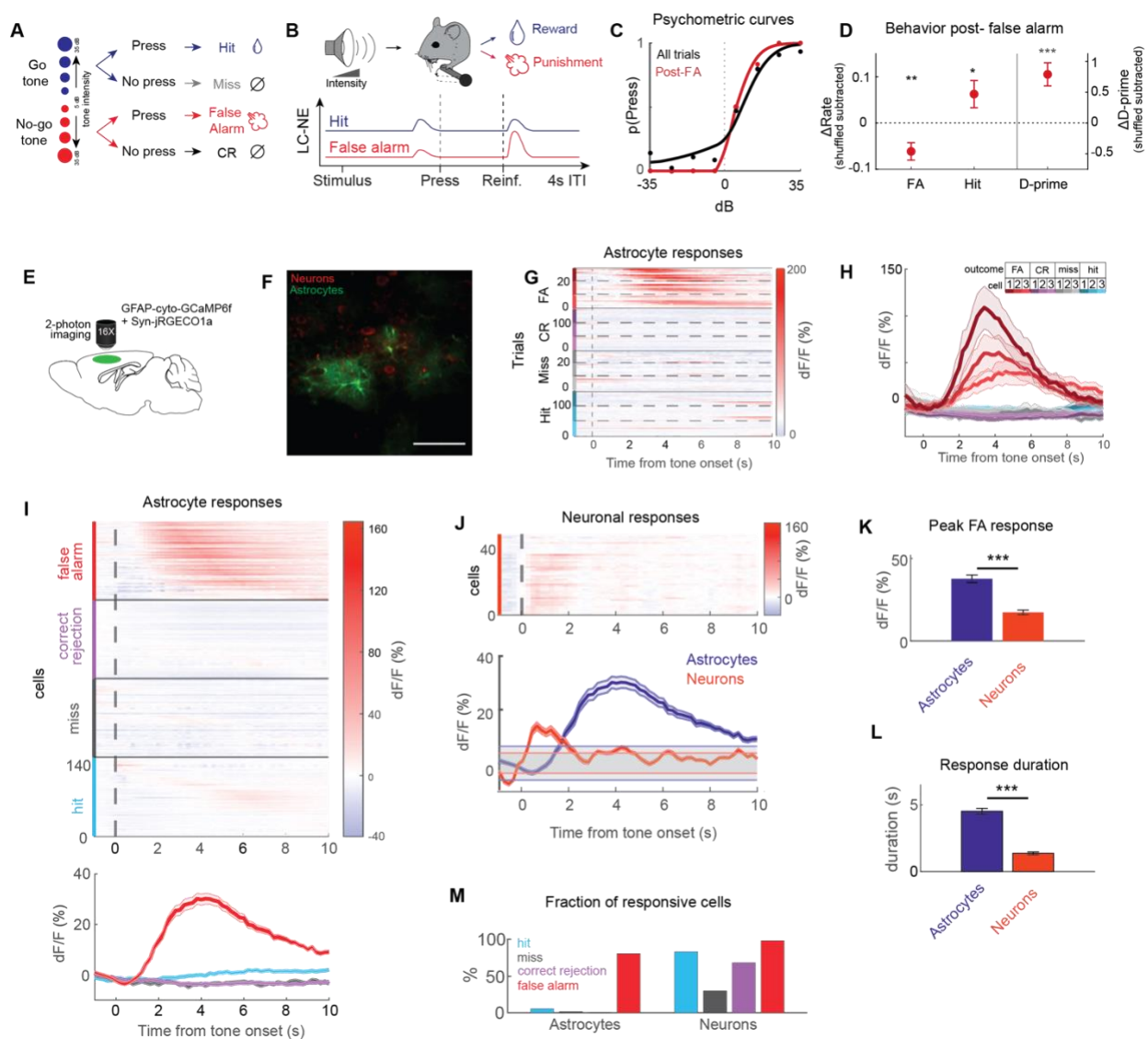
735

Fig 1. Astrocytes exhibit sustained increases in intracellular calcium following a false alarm in a reinforcement learning task. (**A**) Task design. (**B**) Schematic of task and timing/magnitude of LC-NE neuronal activity. ITI, inter-trial interval. (**C**) Example psychometric curves from one mouse showing probability of pressing the lever by tone intensity for all trials (black) and on trials
740   following a false alarm (red). (**D**) Change in false alarm rate, hit rate, and d-prime on trials following a false alarm, calculated after subtracting shuffled data (n=18 mice). P values show comparisons based on two-tailed paired t-test. (**E**) Methods for dual imaging of astrocytes and neurons. (**F**) Example 2-photon image of astrocytes and neurons expressing GCaMP6f and jRGECO1a, respectively. Scale bar = 50 µm (**G**) Mean dF/F of three example astrocytes aligned
745   to tone onset for false alarm (FA), correct rejection (CR), miss, and hit trials. (**H**) Session averaged dF/F for the three example astrocytes aligned to tone onset, by trial type. (**I**) Top: raster plot showing average astrocyte dF/F by trial type, aligned to the time of tone inset. Bottom: average dF/F for all astrocyte ROIs by trial type. n = 148 astrocytes (n = 3 mice). (**J**) Top: raster plot

25

showing average neuronal dF/F on false alarm trials. Bottom: Population average dF/F for all
750 neurons and all astrocytes (from **I**) on false alarm trials, aligned to time of tone onset. Gray zones depict baseline +/- s.d. n = 44 neurons (n = 3 mice) **(K)** Peak dF/F for astrocytes and neurons in response to a false alarm. **(L)** Duration of astrocyte and neuronal responses to a false alarm. **(M)** Fraction of astrocytes (left) and neurons (right) responsive to each trial type. P values show comparisons based on two-tailed unpaired t-test in K, L. *, $p < 0.05$; **, $p < 0.01$; ***, $p < 0.001$.
755 Data show mean +/- SEM.

Figure 2
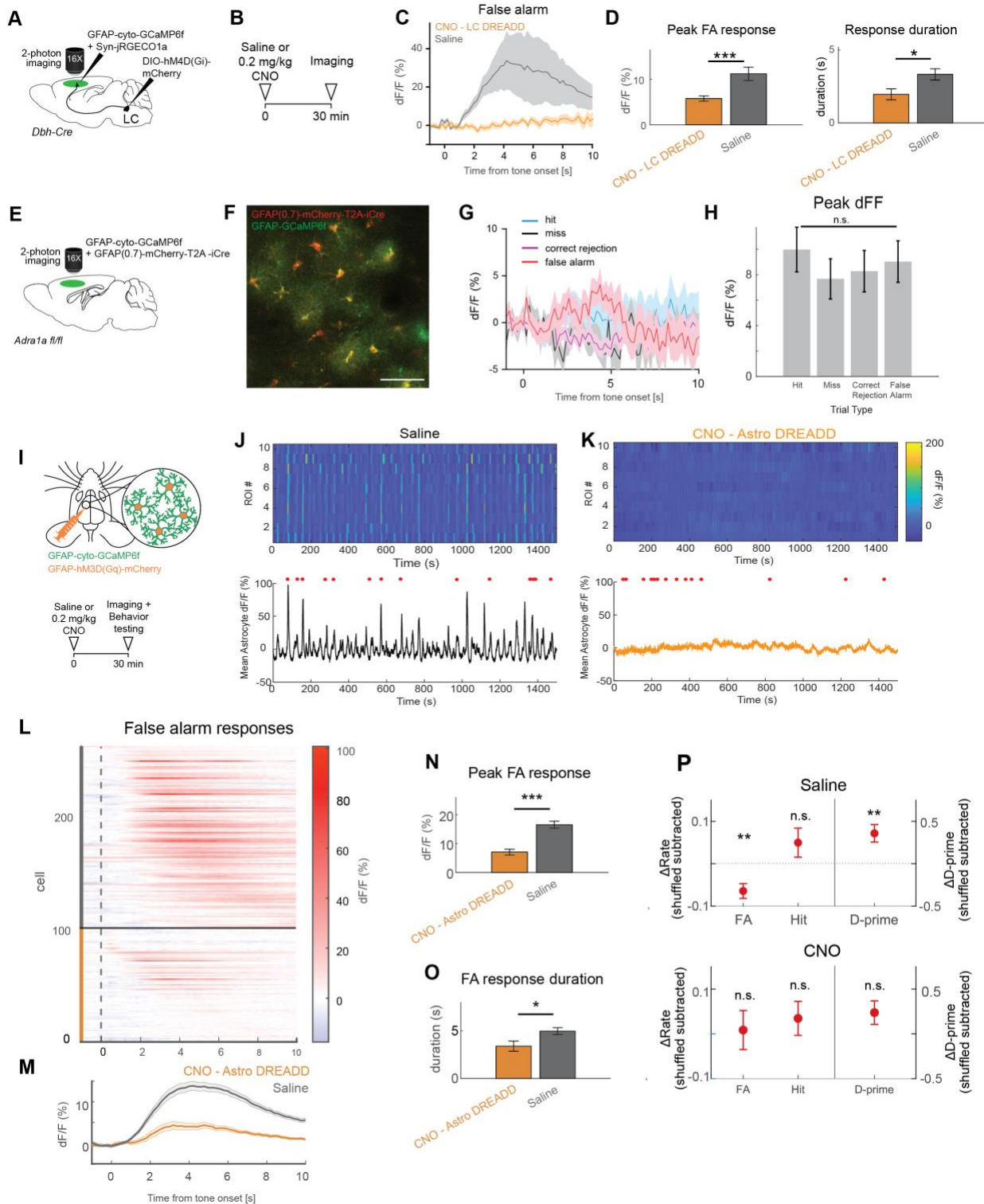
Figure 2. NE and adrenergic receptor-specific responses of astrocytes and effects of manipulating calcium on behavior. A. Experimental design for chemogenetic silencing of LC-

NE neurons while imaging astrocyte calcium. **B.** Experimental timeline. **C.** Example trial averaged astrocyte trace on a false alarm trial for a saline and CNO session. **D.** Left: Average peak astrocyte dF/F on false alarm trials for saline and CNO sessions. Right: Average FA response duration for responsive astrocytes in saline and CNO sessions. CNO, n = 108 astrocytes; saline, n = 101 astrocytes (n = 3 mice). P values show comparisons based on two-tailed unpaired t-test. **E.** Experimental design for imaging astrocyte calcium in astrocytes with Adra1a receptor knockdown. **F.** Example 2-photon image showing overlapping Cre and GCaMP6f expression in astrocytes. Scale bar, 50 um. **G.** Example traces for hit, miss, correct rejection, and false alarm trials from one astrocyte. **H.** Population averages for peak astrocyte dF/F for all trial types in Adra1a-R KD astrocytes. n = 44 astrocytes (n = 3 mice). P value determined using one-way ANOVA. **I.** Experimental design and timeline for chemogenetic manipulation of astrocyte calcium. **J.** Top: Average dF/F for each astrocyte ROI over the course of a saline imaging session. Bottom: population average. Red dots indicate false alarms. **K.** Average dF/F for each astrocyte ROI over the course of a CNO imaging session. Bottom: population average. Red dots indicate false alarms. **L.** Average astrocyte dF/F on false alarm trials for saline (top) and CNO (bottom) sessions. CNO, n = 99 astrocytes; saline, n = 160 astrocytes (n = 5 mice). **M.** Population average from L. **N.** Average peak dF/F for astrocytes in saline and CNO sessions. **O.** Average response duration for responsive astrocytes in saline and CNO sessions. **P.** Change in false alarms (FA), hits, and d-prime on trials after a false alarm for saline (top) and CNO (bottom) sessions (n= 12 mice). P values show comparisons based on two-tailed unpaired t-test in N, O, and two-tailed paired t-test in P. *, p < 0.05; **, p < 0.01; ***, p < 0.001. Data show mean ± SEM.

28
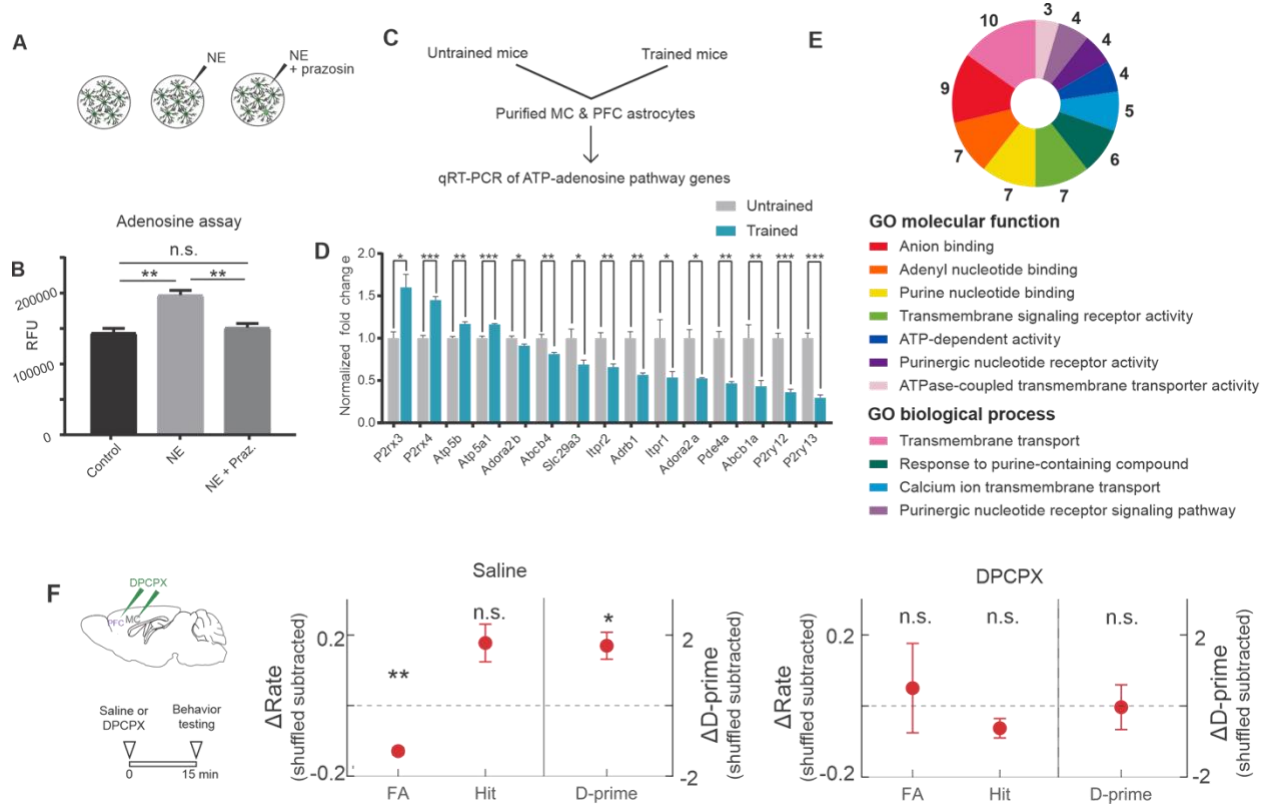
Figure 3

Figure 3. Astrocytes mediate reinforcement learning via purinergic signaling. A. Experimental design of adenosine fluorometric assay of astrocyte cultures. **B.** Adenosine assay showing an increase in adenosine release in response to NE (20 µM) from cultured astrocytes. (n = 3). NE-induced release of adenosine is blocked in the presence of prazosin hydrochloride. (n = 3). RFU = relative fluorescence units. **C.** Schematic for gene expression analysis. **D**. Average gene expression fold change of significantly different genes in trained mice, measured by qRT-PCR and normalized to untrained mice. (untrained mice, n = 4 hemispheres; trained mice, n = 6 hemispheres). **E**. Pie chart showing the functional classification of differentially expressed genes annotated to their GO molecular function and GO biological process terms. The size of each wedge represents the number of significantly changed genes in each functional class, as noted. **F.** (Left) Experimental design applying saline or DPCPX topically to prefrontal and motor cortex followed by behavioral testing. (Center, right) Change in false alarms, hits, and d-prime on trials after a false alarm in saline and DPCPX conditions. P values show comparisons based on two-tailed unpaired t-test in B, D, and two-tailed t-test in F (n=3 mice). *, p < 0.05; **, p < 0.01; ***, p < 0.001. Data show mean + SEM.
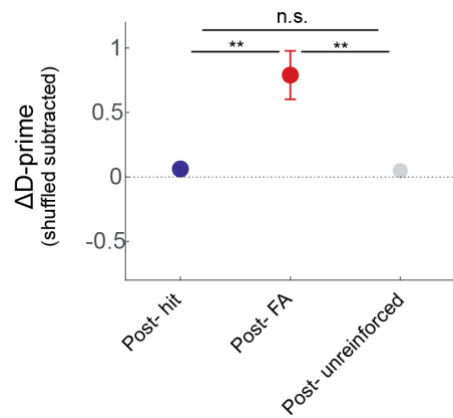
Figure 4

805

Figure 4. Astrocyte calcium manipulations and A1 receptor blockers occlude improvements in neuronal stimulus encoding post- false alarm. A. Experimental design for saline, CNO, and DPCPX recordings. **B.** Top: Rasters showing activity on single trials for go and no-go stimuli after unreinforced (gray) and false alarm (red) trials for example units. Bottom: Average activity for

810   go/no-go stimuli after unreinforced and false alarm trials. **C.** Population averaged firing rate for go and no-go stimuli on trials after a false alarm in saline (top), CNO (center), and DPCPX (bottom) conditions. **D.** Quantification of the difference between go and no-go firing rates on trials after hit (blue), false alarm (red), and unreinforced (gray) trials. **E.** D-prime after false alarm versus d-prime after unreinforced trials for saline, CNO, and DPCPX conditions. Blue dots represent

815   individual units. Regression lines are shown in red with 95% bootstrap CI zone in dark blue. Inset: quantification of d-prime post false alarm versus post-unreinforced trials. **F.** Quantification of d-prime after no reinforcement, false alarm, and hits for saline, CNO, and DPCPX sessions. n = 377 neurons, saline (n = 4 mice); n = 271 neurons, CNO (n = 3 mice); n = 186 neurons, DPCPX (n=3 mice). P values show comparisons based on two-tailed paired t-test in D and E (insets), on

820   bootstrap with replacements in E (slopes), and on two-tailed unpaired t-test in F. *, $p < 0.05$; **, $p < 0.01$; ***, $p < 0.001$. Data show mean ± SEM. **G.** Model of the role of NE-astrocyte-adenosine signaling in learned behavior.
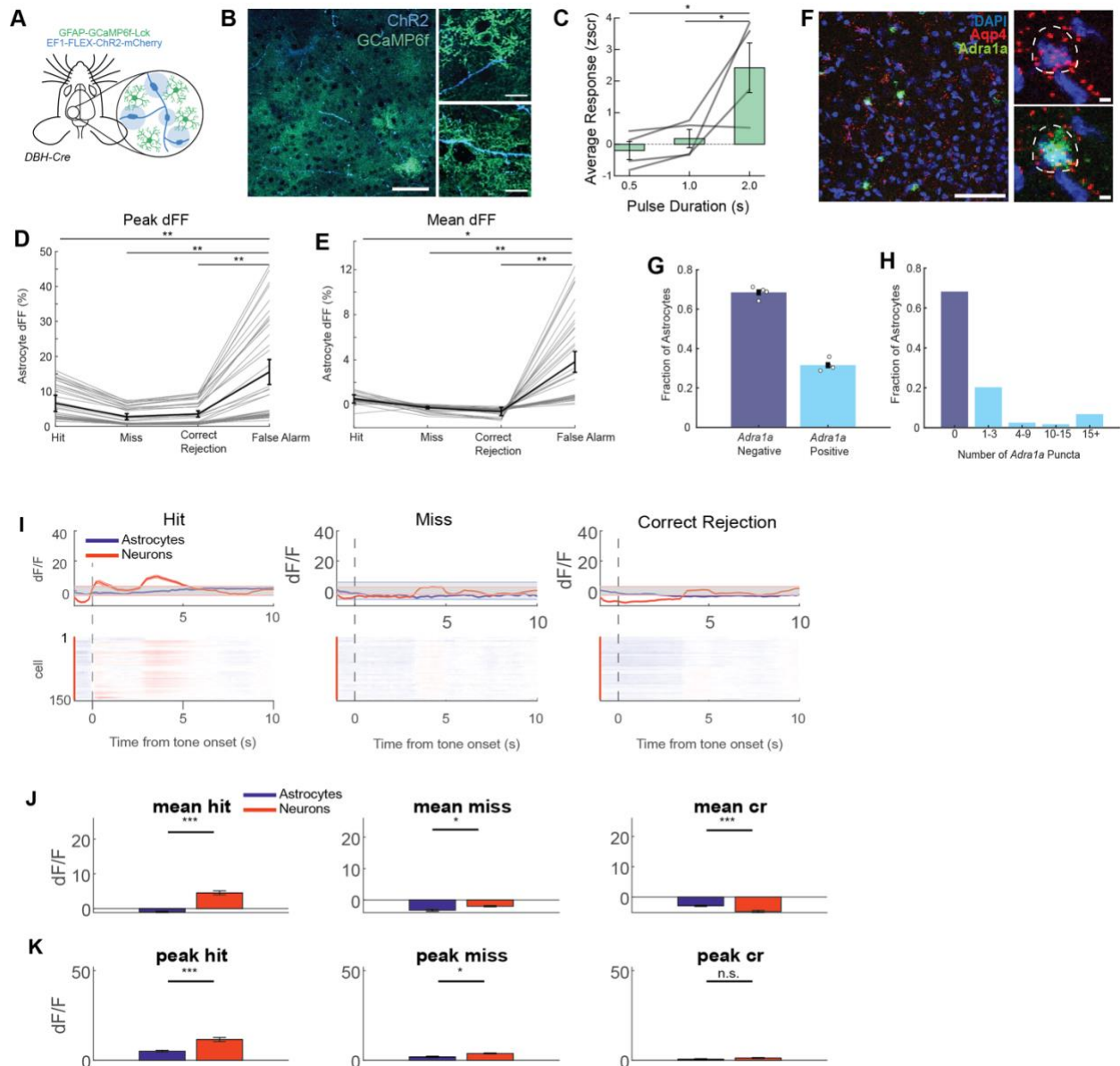
825   **Extended Data Figure 1**

Extended Data Fig. 1. Change in d-prime after hit, false alarm, and unreinforced trials (n = 18 mice). **, $p < 0.01$, two-tailed paired t-test. Data show mean ± SEM.

830

Extended Data Figure 2

Extended Data Fig. 2. **A.** Schematic of experimental design for LC axonal stimulation and astrocyte calcium imaging. **B.** Example 2-photon images of LC axons expressing ChR2 (blue) and astrocytes expressing GCaMP6f (green). Scale bar, left panel, 50 um; right panels, 20 um. **C.** Average astrocyte calcium responses following NE axon stimulation for 0.5, 1.0, and 2.0 seconds. Each gray line indicates data from one animal. Solid bars denote mean, error bars are s.e.m. (n=4 mice). **D.** Peak dF/F for astrocytes during hit, miss, correct rejection, and false alarm trials in go/no-go task. Each gray line indicates one astrocyte. Black line indicates population average, error bars are s.e.m. **E.** Mean dF/F for astrocytes. n = 148 astrocytes (n=3 mice). **F.** Left: Example FISH image of DAPI (blue), aquaporin 4 (Aqp4, red), and Adra1a (green) mRNA expression in the motor cortex. Scale bar: 100um. Right (top): Example astrocyte ROI (dashed line) with overlapping DAPI (blue) and *Aqp4* (red) mRNA expression. Scale bar: 5um. Right (bottom): Same

33

845   as right top, including *Adra1a* (green) mRNA expression. Scale bar: 5um **G.** Quantification of astrocytes (Aqp4+ cells) positive and negative for *Adra1a* transcripts. Each data point represents the fraction for one animal (n=3 mice). **H.** Quantification of Adra1a puncta on astrocytes. **I.** Top: Astrocyte and neuronal population dF/F on hit, miss, and correct rejection trials. Bottom: Rasters of neuronal dF/F on hit, miss and correct rejection trials. Astrocyte rasters are shown in text Fig.

850   1I. n = 148 astrocytes, 44 neurons (n=3 mice). J. Average mean dF/F for hit (left), miss (center), and correct rejection (right) trials for astrocytes and neurons. K. Average peak dF/F for hit, miss, and correct rejection trials for astrocytes and neurons. P values show comparisons based on Mann Whitney U-test in C, two-tailed paired t-test with Bonferroni correction in D and E, two-tailed unpaired t-test in J and K. *, $p < 0.05$; **, $p < 0.01$; ***, $p < 0.001$. Data show mean ± SEM.

855

Extended Data Figure 3
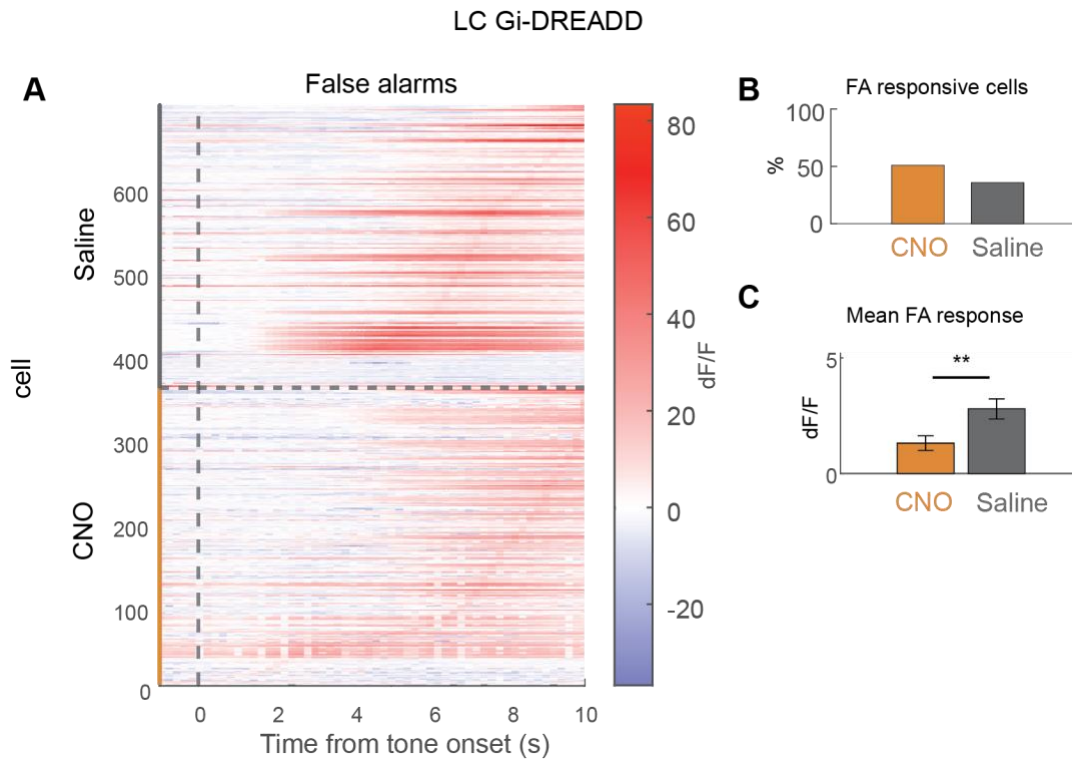
Extended Data Fig. 3. A. Average astrocyte dF/F on false alarm trials for chemogenetic silencing of LC-NE in saline (top) and CNO (bottom) sessions. n = 101 astrocytes, saline; n = 108 astrocytes, CNO (n=3 mice). **B.** Fraction of astrocytes responsive to false alarms in saline and CNO sessions. **C.** Average mean dFF for astrocytes in saline and CNO sessions. **, $p < 0.01$, two-tailed unpaired t-test. Data show mean ± SEM.
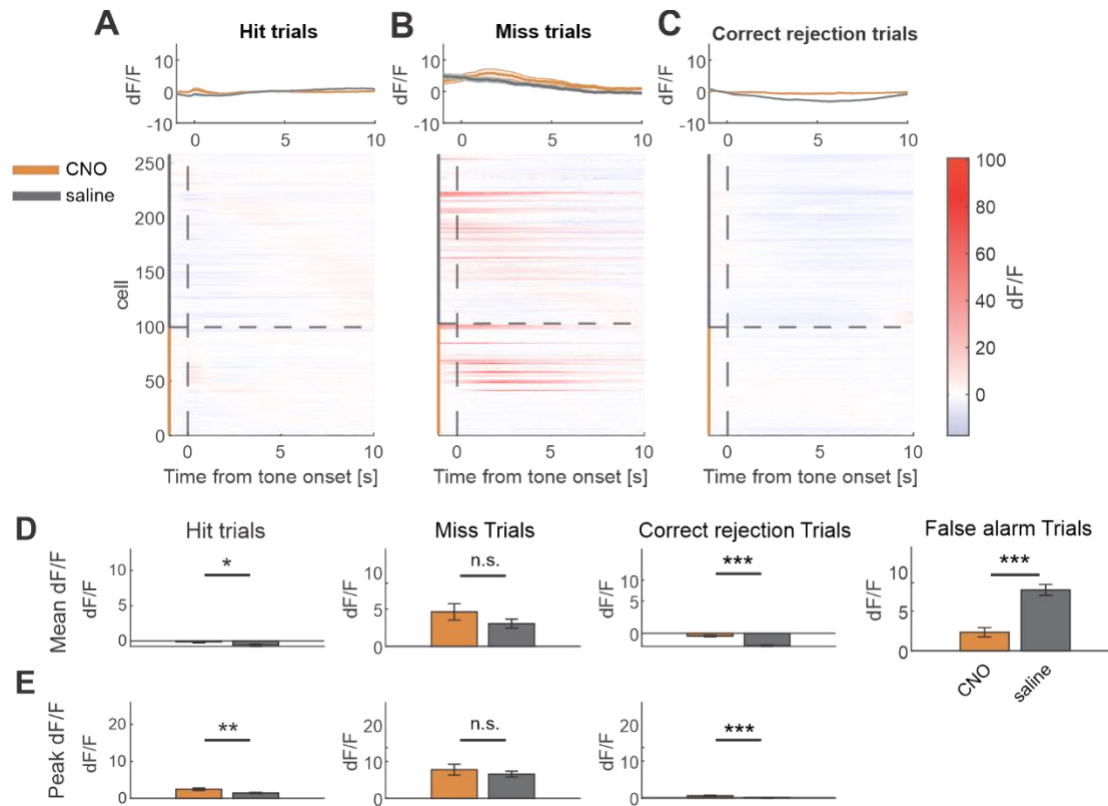
Extended Data Figure 4

865
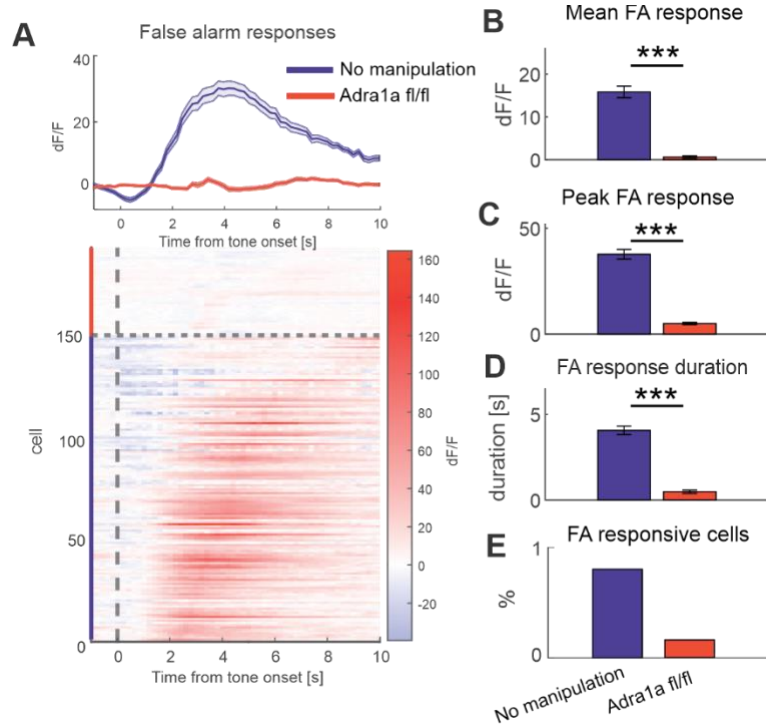
Extended Data Fig. 4. A. Average astrocyte dF/F on false alarm trials without manipulations (blue) and with knockdown of Adra1a receptors (red) sessions; population average (top) and individual cells (bottom). n = 148 astrocytes with no manipulation; n = 44 astrocytes with knock down of Adra1a (n=3 mice). **B.** Average mean dF/F for astrocytes in no manipulation and knockdown of Adra1a sessions. **C.** Average peak dF/F for astrocytes in no manipulation and knockdown of Adra1a sessions. **D.** Average FA response duration for responsive astrocytes in no manipulation and knockdown of Adra1a sessions. **E.** Fraction of astrocytes responsive to false alarms in no manipulation and knockdown of Adra1a sessions. ***, $p < 0.001$, two-tailed unpaired t-test.
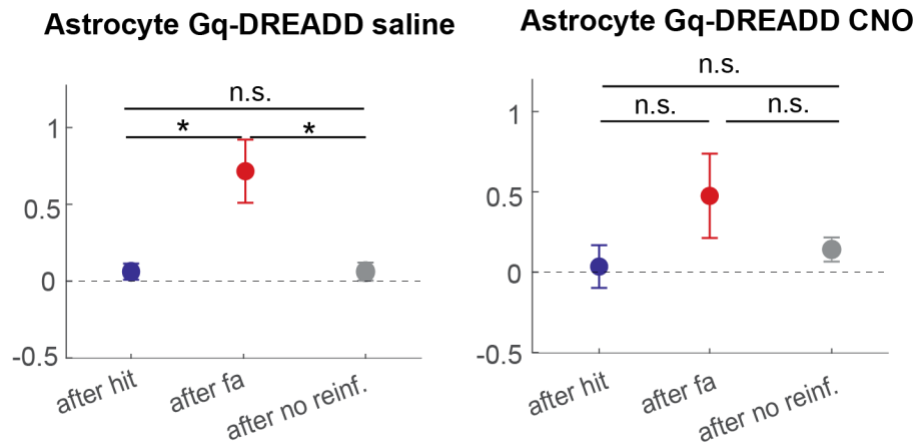
Extended Data Figure 5

Extended Data Fig. 5. A. Average astrocyte dF/F on hit trials for chemogenetic inactivation of astrocytes in saline (gray) and CNO (orange) sessions; population average (top) and individual cells (bottom). n = 160 astrocytes, saline; n = 99 astrocytes, CNO (n = 5 mice). **B.** Same as A on miss trials. **C.** Same as A on correct rejection trials. **D.** Average mean dF/F for astrocytes in saline and CNO sessions for, from left to right: hit, miss, correct rejection, and false alarm trials. **E.** Average peak dF/F for astrocytes in saline and CNO sessions, from left to right: hit, miss, and correct rejection trials. P values show comparisons based on two-tailed unpaired t-test in D and E. *, p < 0.05; **, p < 0.01; ***, p < 0.001. Data show mean ± SEM.
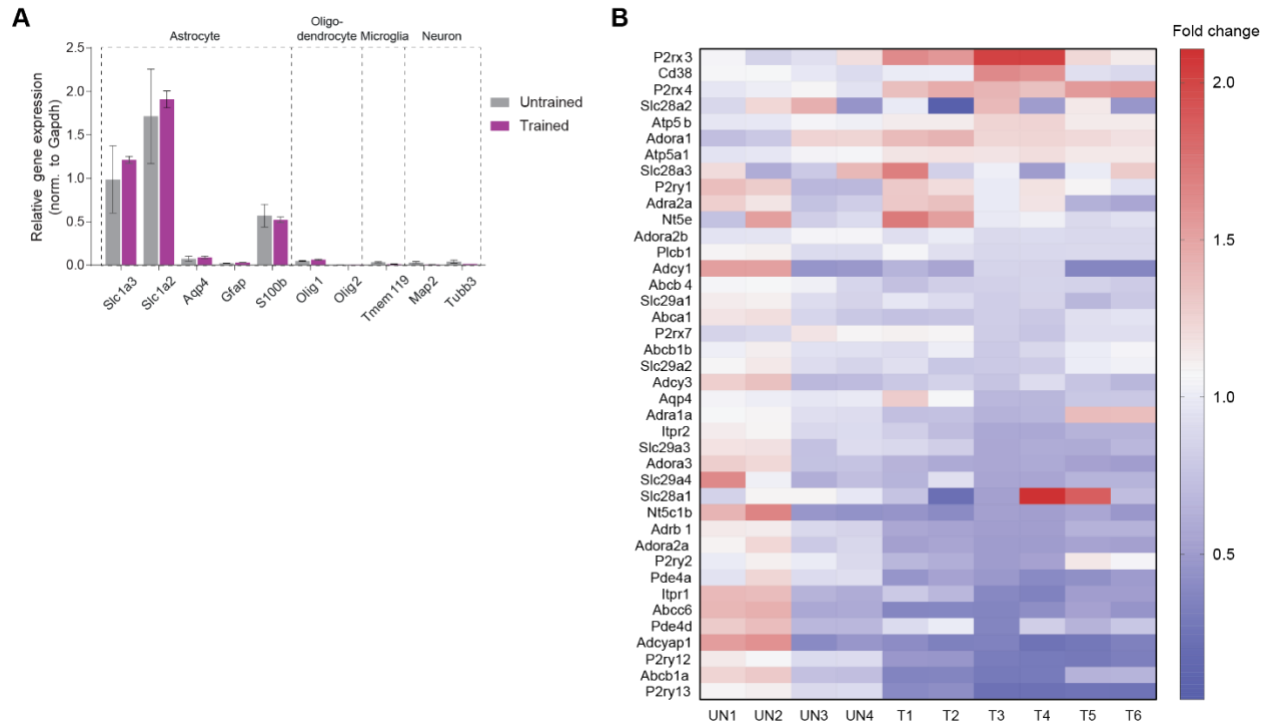
37

Extended Data Figure 6

890

Extended Data Fig. 6. Change in d-prime after hit, false alarm, and unreinforced trials for saline (left) and CNO (right) sessions in astrocyte Gq-DREADD expressing animals (n = 12 mice). *, $p < 0.05$, one-tailed paired t-test. Data show mean ± SEM.

895

38

Extended Data Figure 7

900

Extended Data Fig. 7. A. Purity of isolated astrocytes was confirmed for both untrained and trained animals by measuring the expression of cell-type specific markers for astrocytes (Slc1a3, Slc1a2, Aqp4, Gfap, S100b), oligodendrocytes (Olig1, Olig2), microglia (Tmem119), and neurons (Map2, Tubb3). Gene expression was normalized to Gapdh. Bars represent mean ± SEM. **B**. Heat map of gene expression fold change for 40 selected ATP/ adenosine pathway genes. 15 genes that were significantly different in trained mice compared to untrained mice are shown in Fig. 3D. UN, untrained animals, T, trained animals; UN1-4 and T1-6 represent independent hemispheres.

905

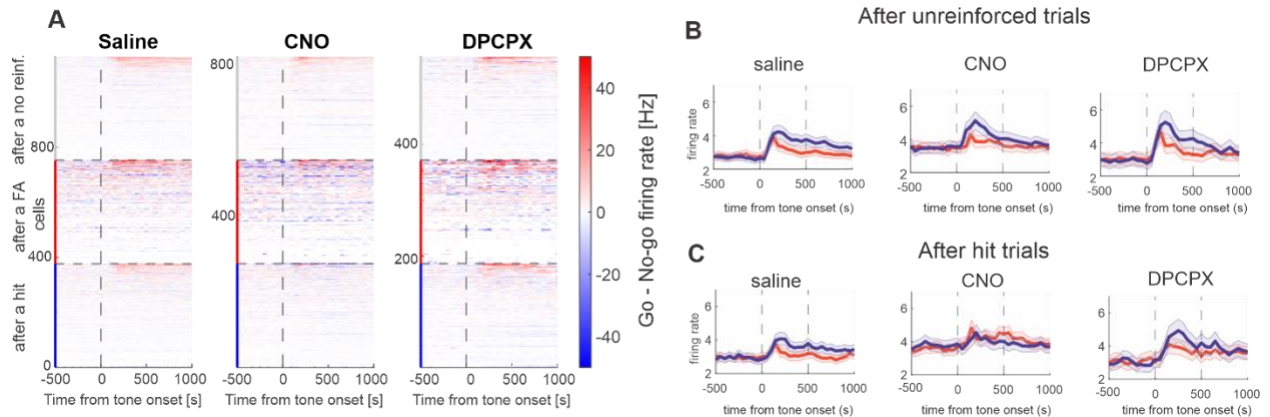39

Extended Data Figure 8
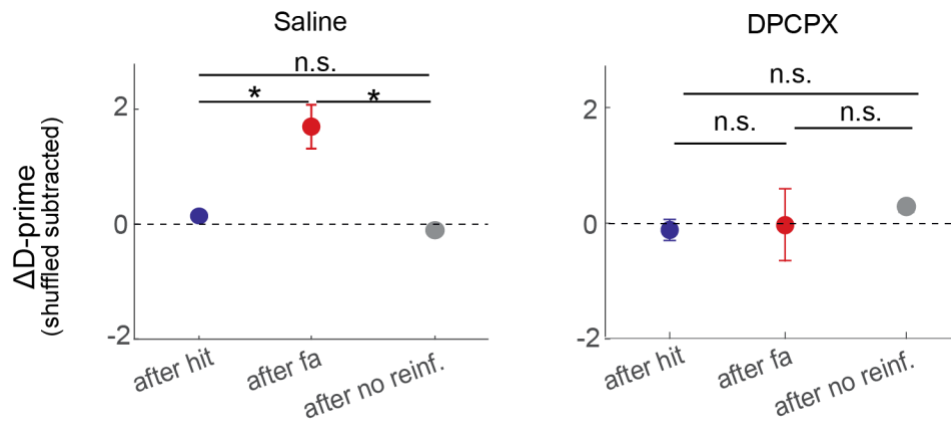
Extended Data Fig. 8. Change in d-prime after hit, false alarm, and unreinforced trials for saline (left) and DPCPX (right) sessions (n = 3 mice). *, $p < 0.05$, one-tailed paired t-test.. Data show mean ± SEM.

Extended Data Figure 9

Extended Data Fig. 9. A. Average neuron firing rate difference between go and no-go trials after hit, false alarm or unreinforced trials for saline (left), CNO (center), and DPCPX (right) sessions. Saline, n = 377 neurons (n = 4 mice); CNO, n = 271 neurons (n = 3 mice); DPCPX, n = 186 neurons (n=3 mice). **B.** Average neuron firing rate for go and no-go stimuli following unreinforced trials in saline (left), CNO (center) and DPCPX (right) sessions. **C.** Same as B following hit trials.

Extended Data Table 1

930

Gene	Forward primer	Reverse primer
Abca1	GCTTGTTGGCCTCAGTTAAGG	GTAGCTCAGGCGTACAGAGAT
Abcb1a	CAGCAGTCAGTGTGCTTACAA	ATGGCTCTTTTATCGGCCTCA
Abcb1b	CTGTTGGCGTATTTGGGATGT	CAGCATCAAGAGGGGAAGTAATG
Abcb4	CAGCGAGAAACGGAACAGCA	TCAGAGTATCGGAACAGTGTCA
Abcc6	TGCGGCCTATCACTTGCTC	CCAGCACCATTTTGGTTTTGAA
Adcy1	GTCACCTTCGTGTCCTATGCC	TTCACACCAAAGAAGAGCAGG
Adcy3	CTCGCTTTATGCGGCTGAC	ACATCACTACCACGTAGCAGT
Adcyap1	ACCATGTGTAGCGGAGCAAG	CTGGTCGTAAGCCTCGTCT
Adora1	TGTGCCCGGAAATGTACTGG	TCTGTGGCCCAATGTTGATAAG
Adora2a	GCCATCCCATTCGCCATCA	GCAATAGCCAAGAGGCTGAAGA
Adora2b	AGCTAGAGACGCAAGACGC	GTGGGGGTCTGTAATGCACT
Adora3	ACGGACTGGCTGAACATCAC	AGACAATGAAATAGACGGTGGTG
Adra1a	CCAGTGTCTTCGCAGAAGG	CAGCAGCAGACCTGCAAAAA
Adra2a	GTGACACTGACGCTGGTTTG	CCAGTAACCCATAACCTCGTTG
Adrb1	CTCATCGTGGTGGGTAACGTG	ACACACAGCACATCTACCGAA
Aqp4	CTTTCTGGAAGGCAGTCTCAG	CCACACCGAGCAAAACAAAGAT
Atp5a1	TCTCCATGCCTCTAACACTCG	CCAGGTCAACAGACGTGTCAG
Atp5b	GGTTCATCCTGCCAGAGACTA	AATCCCTCATCGAACTGGACG
Cd38	TCTCTAGGAAAGCCCAGATCG	GTCCACACCAGGAGTGAGC
Gapdh	AGGTCGGTGTGAACGGATTTG	TGTAGACCATGTAGTTGAGGTCA
Gfap	CGGAGACGCATCACCTCTG	AGGGAGTGGAGGAGTCATTCG
Itpr1	CGTTTTGAGTTTGAAGGCGTTT	CATCTTGCGCCAATTCCCG
Itpr2	TTCAGTTCCTATCGAGAGGATGT	GCTGATTGACGCAAGGTCG

42

Map2	GCCAGCCTCGGAACAAACA	GCTCAGCGAATGAGGAAGGA
Nt5c1b	CTGCCATCAAGGCCCCTAAC	GCATCCCTTCTCGTGAGTCA
Nt5e	GGACATTTGACCTCGTCCAAT	GGGCACTCGACACTTGGTG
Olig1	TCTTCCACCGCATCCCTTCT	CCGAGTAGGGTAGGATAACTTCG
Olig2	TCCCCAGAACCCGATGATCTT	CGTGGACGAGGACACAGTC
P2rx3	AAAGCTGGACCATTGGGATCA	CGTGTCCCGCACTTGGTAG
P2rx4	CTGGTGTGCCAACGAGGAATA	AGACGGAATATGGGGCAGAAG
P2rx7	GACAAACAAAGTCACCCGGAT	CGCTCACCAAAGCAAAGCTAAT
P2ry1	GAGGTGCCTTGGTCGGTTG	CGGCAGGTAGTAGAACTGGAA
P2ry12	ATGGATATGCCTGGTGTCAACA	AGCAATGGGAAGAGAACCTGG
P2ry13	ATGCTCGGGACAATCAACACC	GATGTGGACGAACACCCAGAG
P2ry2	CTGGAACCCTGGAATAGCACC	CACACCACGCCATAGGACA
Pde4a	AATGCCCTACAGACGCCTG	GACGGTGTTGGCCCATTTT
Pde4d	AACACTGCACTCCTGTAATGAAG	TGCTTGTTCCAACTGTCTGAAG
Plcb1	GCCCCTGGAGATTCTGGAGT	GGGAGACTTGAGGTTCACCTTT
S100b	TGGTTGCCCTCATTGATGTCT	CCCATCCCCATCTTCGTCC
Slc1a2	GCACGAGAGCTATGGTGTATTAC	GTTTGGGATTACCTGGGTGGA
Slc1a3	ACCAAAAGCAACGGAGAAGAG	GGCATTCCGAAACAGGTAACTC
Slc28a1	GATCTTGTGGCTATCTCTGGACA	ACGCAACGAATCCTGGCTC
Slc28a2	AGTGGAGAATTGCATGGAGAAC	GACCAAGCAGGATCTTTCTGAA
Slc28a3	GACCTTGAACGGCAGAACACT	CTTTGTTTCCTAGAGGCTCCTG
Slc29a1	CAGCCTCAGGACAGGTATAAGG	GTTTGTGAAATACTTGGTTGCGG
Slc29a2	TCATTACCGCCATCCCGTACT	CCCAGTTGTTGAAGTTGAAAGTG
Slc29a3	GAGCCCCGAGTAACCATCAAG	CATTGAAGCGATCCTCTGGC
Slc29a4	CACAGACTCTGCGGTAGAGGA	CCTGGGTACTTGTGGTGAAGATA
Tmem119	CCTACTCTGTGTCACTCCCG	CACGTACTGCCGGAAGAAATC

43

Tubb3	TAGACCCCAGCGGCAACTAT	GTTCCAGGTTCCAAGTCCACC

Extended Data Table 1. List of primers used for qRT-PCR.